OPEN ACCESS
Journal of Multidisciplinary Applied Natural Science Vol. 5 No. 1 (2025) https://doi.org/10.47352/jmans.2774-3047.227
Check for updates
Research Article

Characterization of the Small Robotic Telescope Instrument and Implementation at ITERA Lampung Astronomical Observatory

Hakim L. Malasan*, Robiatul Muztaba, Aditya Abdillah Yusuf, Adhitya Oktaviandra, Mitra Djamal, Tulin Bedel, Peter Aniol

Received : June 29, 2024	Revised : September 13, 2024	Accepted : September 20, 2024	Online : October 9, 2024

Abstract
As time has passed, the technological advances used to run these telescope systems have become faster, more reliable, and more user-friendly. Institut Teknologi Sumatera (ITERA) has installed a small robotic telescope at the Meteorology–Climatology–Geophysics Observing Station in collaboration with an ASTELCO System. The telescope system is designed to make fully robotic observations and can operate in both interactive and unattended robotic modes. This study's primary focus is on the OZT-ALTS telescope robotic system with the optical system using triplet apochromatic lens technology manufactured by LZOS with a focal ratio of f/8 refractor design. The telescope mount is a German Equatorial (NTM-500 manufactured by ASTELCO) with a direct drive system with an absolute encoder, and it allows fully programmable tracking speeds with a typical slewing speed of 20°/sec and a tracking accuracy range of 0.3–1.0 arcsec. For the process of collecting moon observation images, we use Manta G-031B. The OZT-ALTS robotic telescope is now contributing to monitoring crescent moon observation and astronomical studies. This paper presents the scientific motivation behind the OZT-ALTS robotic telescope and the facility's specifications and unique features. Furthermore, we present to characterize the result of the hardware OZT-ALTS robotic telescope system to increase the mechanical and optical performance of the telescope system based on the in-situ test observations. Based on the result, setting the Gain on the camera at 3.5 e-/ADU is the limit for the CCD to produce good-quality output images by utilizing the entire dynamic range without saturation. We also present an example of the science we have performed with the OZT-ALTS robotic telescope. The OZT-ALTS can observe young crescent moon events in the daylight after implementing the CLAHE technique to enhance contrast objects. On the other hand, the OZT-ALTS can also observe WASP-16b and WASP-34b exoplanets by using the transit method to analyze the decreasing light curve when a planet passes between a star and its observer.

Keywords: optics, photonics, light, telescopes, characterize

1. INTRODUCTION

In early 2020, Institut Teknologi Sumatera (ITERA) and ASTELCO Systems collaborated to develop a sustainable crescent observation program using a robotic telescope designed and manufactured by ASTELCO Systems. However, due to the Coronavirus (COVID-19) outbreak, the installation and commissioning process was delayed until November 2021. During November and December 2021, The Tower and Telescope were successfully installed at the Meteorology–Climatology–Geophysical Observing Station with geographic coordinates of 5° 21' 45.9"S and 105° 18' 41.7"E, at 90 m above sea level, the telescope was fine-tuned both mechanically and optically. This robotic telescope produced by ASTELCO Systems is specially designed to optimize the observation of the crescent moon, which has problems with the contrast between the crescent moon and the sky background [1]. Therefore, besides being able to observe at visual wavelengths, this telescope is equipped with a sensitive RG1000 infrared filter to capture very thin and faint crescent objects, making it easier to observe the crescent moon. To characterize a camera based on a CCD detector, we need to identify sources that can produce artifacts in an image. Artifacts in an image result from the contributions of noise components, effective Gain, conversion factor, linearity, modulation transfer function, and detective quantum efficiency. The noise itself is divided into several types, namely temporal noise, which can change randomly from image to image. Temporal noise includes stochastic contributions such as dark current noise, readout noise, photon noise, beam flicker, burst noise, and shutter noise. There is also fixed-pattern noise, such as dust, CCD bias patterns, and other artifacts that produce pixel-to-pixel sensitivity variations and distortion in the optical path to the CCD or the CCD chip itself [2].

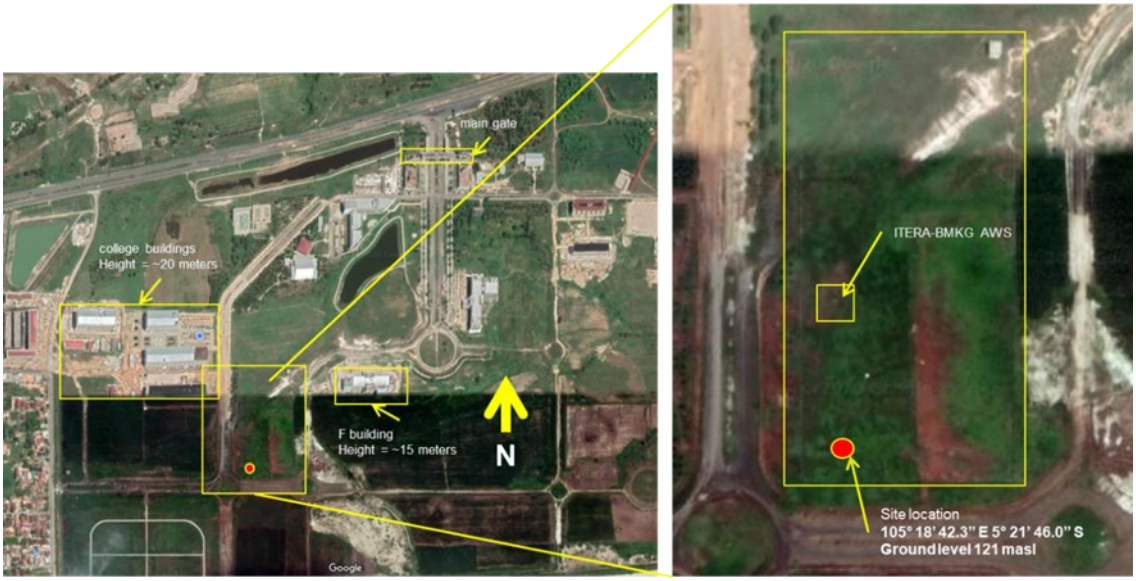

Figure 1. Site Location of OZT–ALTS robotic telescope in ITERA Campus.

Figure 2. The OZT-ALTS robotic telescope at ITERA Lampung Astronomical Observatory.

The ASTELCO Lunar Telescope System (ALTS) built at ITERA will complement the International Moon Sighting Station (IMSS). The observation station is included in a major project currently being worked on by ASTELCO in several countries in the world. A total of 14 similar observation stations have been established in several countries, such as Saudi Arabia, Hawaii, Mexico, and Morocco, and now one of them will be at ITERA Lampung. The collaborative research between ITERA and ASTELCO on moon sightings holds great importance, particularly for Muslims, in accurately establishing the commencement of the Hijri month in the Islamic calendar. The continuous monitoring of the crescent moon will be conducted using the OZT-ALTS robotic telescope, which can enhance the precision and accuracy of moon observations, enabling the development of a more accurate calendar system.

In this paper, we present the design and manufacture of the system and introduce the default configuration and modified system design and setting to measure the performance of the mechanical and optical quality of the telescope system based on the results of test observations using some moon crescent, and exoplanet. Since the

beginning of 2022, a robotic telescope called OZT-ALTS has been actively operating, making various astronomical observations, especially the crescent moon [3][4]. In 2009, Lister et al. used transit and radial velocity analysis to confirm the physical parameters of WASP-16 b [5]. In 2013, Southworth used the Danish telescope to obtain four transits of WASP-16 b to improve its physical and ephemeris parameters [6]. Furthermore, Knutson [7], Stassun [8], and Bonomo [9] will continue to improve physical parameters, reaching Patel in 2022 [10]. Meanwhile, Smalley et al. confirmed the physical parameters of WASP-34 b, concluding that other objects are orbiting the system with long orbital periods [11]. The paper by Knutson, Bonomo, and Stassun also included ephemeris updates and exoplanet parameters. We determined several exoplanet parameters and compared them to the literature study.

2. METHODS

2.1. Configuration Telescope System

The OZT-ALTS is located in ITERA, Lampung, Indonesia, with geographic coordinates of 5° 21' 45.9"S, 105° 18' 41.7"E, at 90 m above sea level as seen in Figures 1 and 2. The telescope is mounted on a concrete pillar with a German NTM-500 equatorial mount and a steel tower on a rock outcrop. The pier's height is approximately 4 m, and the total rock outcrop with steel towers is approximately 3 m above ground level. Additionally, the telescope is protected by a folding -type dome from the manufacturer ASTELCO. The instrument concept is based on a multi-wavelength approach, involving a set of instruments with two cameras working at a visual and infrared wavelength to monitor and observe the moon. This strategy optimizes the number of targets observed at a given noise level and their contrast. The sky camera and cloud sensor will be mounted around the dome, resulting in a continuous survey of the same region of the sky.

The OZT-ALTS hardware system was designed by ASTELCO Systems GmBH (Munich, Germany) and was installed at ITERA in December 2021. The telescope used in OZT-ALTS is a refracting telescope with a triplet apochromatic lens with a lens diameter of 152 mm, focal length of 1200 mm, and Strehl ratio of 0.97. The optical system is outfitted with the Optec TCF-Si and combined with a German NTM-500 equatorial mount and two high

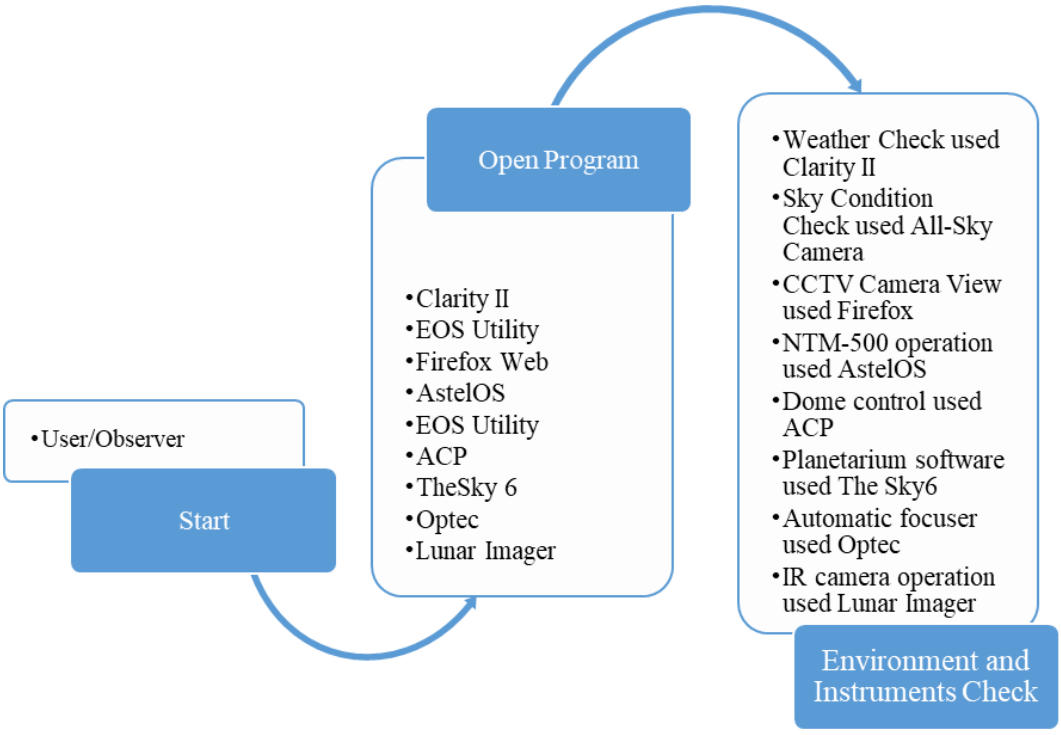

Figure 3. OZT–ALTS remote operation procedure.

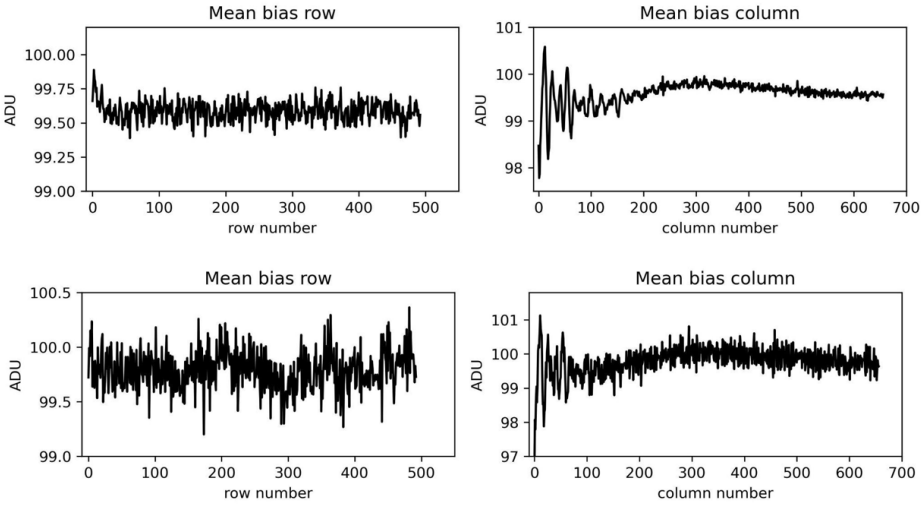

Figure 4. Signal fluctuations in image rows and columns: Upper panels for Gain = 0 and lower panels for Gain = 2.

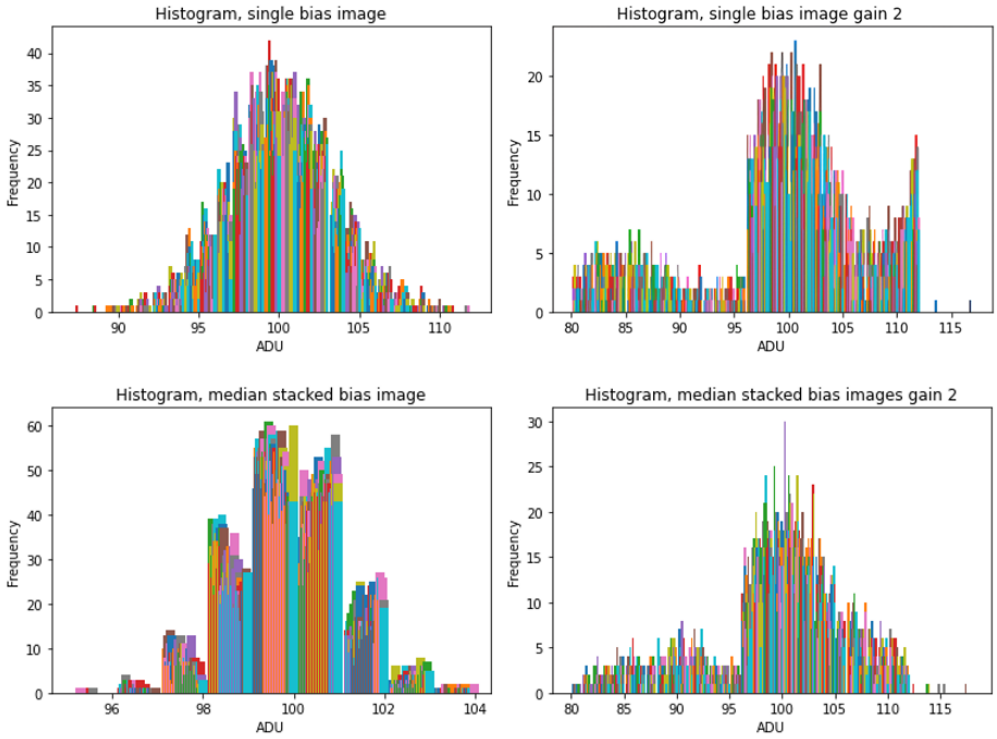

Figure 5. A biased image histogram for a single image and a set of images: Left Panels for gain= 0, right panels for gain = 2.

-sensitivity video cameras: a CCD camera (Manta G -031B) and a DSLR camera (Cannon EOS 5D Mark II). Manta G-031B has an exposure time of 58 µsec to 60 sec with a max of 125 fps and, in this system, has a 21×15 arcsec field-of-view. Meanwhile, the Cannon EOS 5D Mark II has an exposure time of 1/8000 sec to 30 sec. This system is equipped with a Baader Fluorite Flatfield Converter (FFC) at 2200 mm focal length, 56×37 arcmin field of view, and 0.6 arcsec/pix.

Furthermore, the front of the Manta G-031B is outfitted with an infrared channel filter, such as the RG 1000, to improve the chances of detecting the crescent moon. The OZT-ALTS is operated with ACP Observatory Control. The operator can either write observing plans and upload them to each station or let each station run autonomously. In this mode, the station decides by itself (depending on

weather conditions and if the moon is available) whether to open the enclosure, point to the moon, take images, upload images to the web, and close the enclosure again. The schematic OZT – ALTS robotic telescope remote procedure is shown in Figure 3.

2.2. Characterization of Manta G-031B

This in-situ characterization was carried out using the most common method, namely the photon transfer method [12]. Janesick's book on photon transfer is an excellent resource for those seeking a complete discussion of this topic [13]. In this method, the signal variance is related to the average signal the CCD chip receives. Various images with different signal strengths can be obtained by varying the integration time of screen imaging with uniform light intensity. From the compiled photon transfer curve, we can obtain the basic parameters of CCD cameras, such as the effective number of bits, the effective Gain, the readout noise, the full well capacity, and the dynamic range. This calculation was also performed on Abbott [14].

3. RESULTS AND DISCUSSIONS

3.1. Characterization of Manta G-031B

The Manta G-031B camera characterization results are as follows: The Manta G-031B is a Gigabit Ethernet (GigE) camera with high-speed data transfer with the ICX618 sensor. The ICX618 sensor is a type of EXview HAD CCD with high sensitivity in the visible and near-infrared (NIR) spectra. Based on the technical specifications mentioned above. We present the results of the in situ characterization of this camera based on the characteristics of the observatory environment and the needs of astronomical observations. Camera performance testing is carried out at night and varies the gain value at the initial camera settings. The goal is to understand digitization noise and see how much impact it has on improving the signal. In

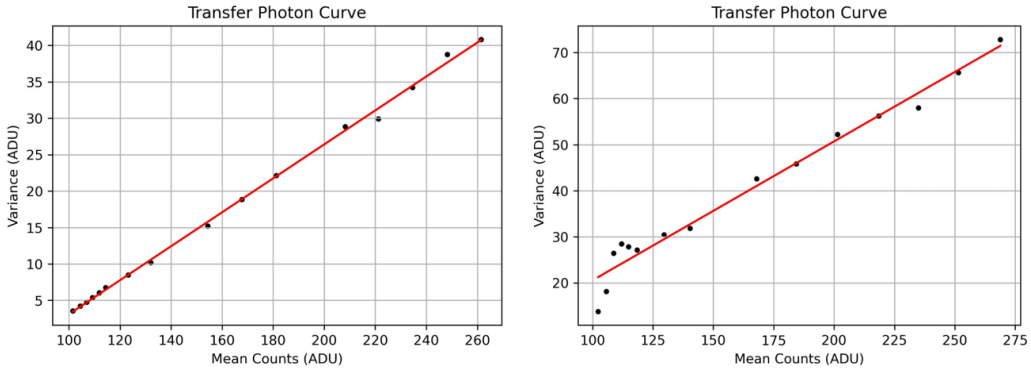

(a) (b)

Figure 6. (a) Photon transfer curve display with a gain = 0, and (b) camera device gain = 2.

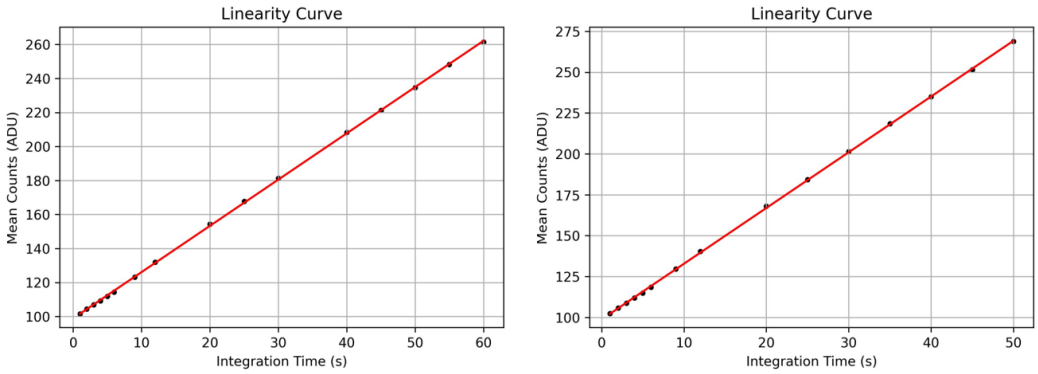

(a) (b)

Figure 7. (a) Linearity curve with m = 2.72 and R^2 = 0.99, (b) linearity curve with m = 3.41 and R^2 = 0.99.

Table 1. Parameter values for the characterization of the Manta G-031B Camera.

Properties	Value-based on manufactures	Value with Set Gain = 0	Value with Set Gain = 2
M	0.22	0.23	0.30
Constant	-	20.22-	9.60-
Conversion Factor (K)	-	4.29 e-/ADU	3.32 e-/ADU
Readout Noise from Intercept Method	11.73 e-/pix	19.29 e-/pix	10.28 e-/pix
Readout Noise from a Bias Image	11.73 e-/pix	12.39 e-/pix	22.88 e-/pix
Full Well Capacity	14508 e-	17563.0 e-	13582.0 e-
Dynamic Range	4096–3600	1417.74	593.42
Dynamic Range in dB	61.49	63.00	55.50
Effective Number of Bit	12.0	10.5	9.2

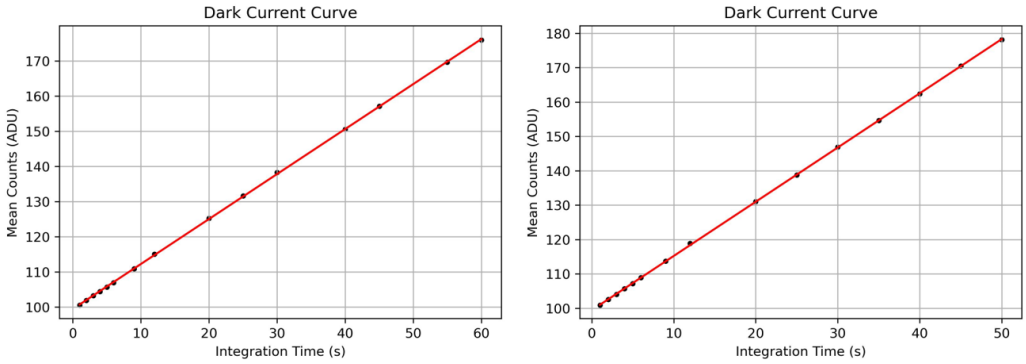

(a) (b)

Figure 8. (a) Dark current as a function of integration time with the gain = 0, and (b) with the gain = 2.

determining the intrinsic parameters of the camera, we refer to the method that has been used by Jannesick and Abbott. First, we use the bias image to identify the uniformity of the signal distribution for each pixel and calculate the zero noise level reading taken with a very short exposure time close to zero without any exposure to light (shutter closed). In principle, the zero bias level may still apply after an overscan correction. This zero-level calibration is obtained by taking an image with zero integration time. In other words, this level considers the active pixel's electronic offset. Several zero-bias images must be taken and then properly combined to get an average zero-bias image. In our case, the Manta G-031B device only allows 58 µs as a minimum integration time, which is close to zero. Figure 4 shows the signal fluctuations in the rows and columns of the image plane. Signal fluctuations that occur in the imaging area are caused by the ability of each pixel to capture different signals depending on the resistivity level of each pixel. The electrons captured in the camera pixel depend on the voltage applied during integration to hold them where the pixel is.

Readout noise generally indicates the number of electrons inserted per pixel into the final output signal. Read noise consists of two inseparable components. The first is converting analogue signals to digital numbers, which cannot be repeated perfectly. Each amplifier on the CCD chip (depending on the gain setting on the camera device) and the DN circuit will produce a statistical distribution centered on the mean value. Second, the electronics themselves will introduce fake electrons into the entire process, resulting in unwanted random fluctuations in the final output. These two effects combine to produce additive uncertainty in the final output value for each pixel. The average level of uncertainty is what is referred

to as readout noise, and it also depends on the gain setting on the camera device.

Figure 4 (upper panels) represent graph of row and column signal fluctuations at the device gain setting equal to zero, while Figure 4 (lower panels) show signal fluctuations at device settings with gains equal to two. From these experiments, we conclude that if the gain is increased, the signal will increase for each pixel along the row and column. The readout noise value is 12.39 e-/pix for a gain setting equal to zero and 22.89 e-/pix for a gain setting equal to 2. To make it easier to understand how different gain settings can change the signal, we present it as a graph of the signal frequency histogram against the signal value. Figure 5 is based on identifying the histogram on one image and the resulting image of more than one (stacking images); both have the same pattern. The histogram at the gain setting of zero shows a uniform signal distribution throughout the image plane with the highest peak value of 98.6 ADU, but the results are different when the Gain is set to 2. When the Gain is set to 2, signals with values >100 dominate more throughout the image plane.

Furthermore, the photon transfer curve is a standard method used to determine the characteristics of a CCD by evaluating the photo-electron statistics detected by a CCD camera. The input from the CCD camera is in the form of photons coming towards the CCD, while the output is in the form of a signal in DN or Analog-Digital Unit (ADU) units obtained by encoding the signal at each pixel. Therefore, a conversion factor is needed to convert the output signal unit in DN into a more representative physical quantity, in this case, the number of photo-electrons. This conversion factor is denoted as the constant K in units of electrons/DN. The K constant can be obtained from the transverse photon curve, which is plotted either linearly or semi-logarithmically. The photon transfer curve can be used to measure the camera's performance characteristics empirically. The photon transfer curve is in the form of a linear graph or the form of the total image noise (standard deviation of

Table 2. CCD Parameters derived from the dark current curve.

Properties	Value with Gain = 0	Value with Gain = 2
Gradient	1.28	1.58
Intercept	99.45	99.43
R Square	0.99	0.99
Dark Current	5.49e-/sec/pix	5.23e-/sec/pix
Bias Level	426.53e-/pix	329.78e-/pix

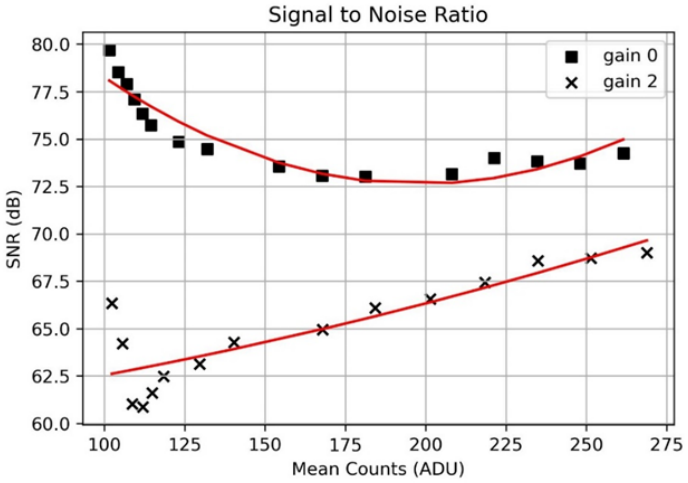

Figure 9. Graphs of signal-to-noise ratio.

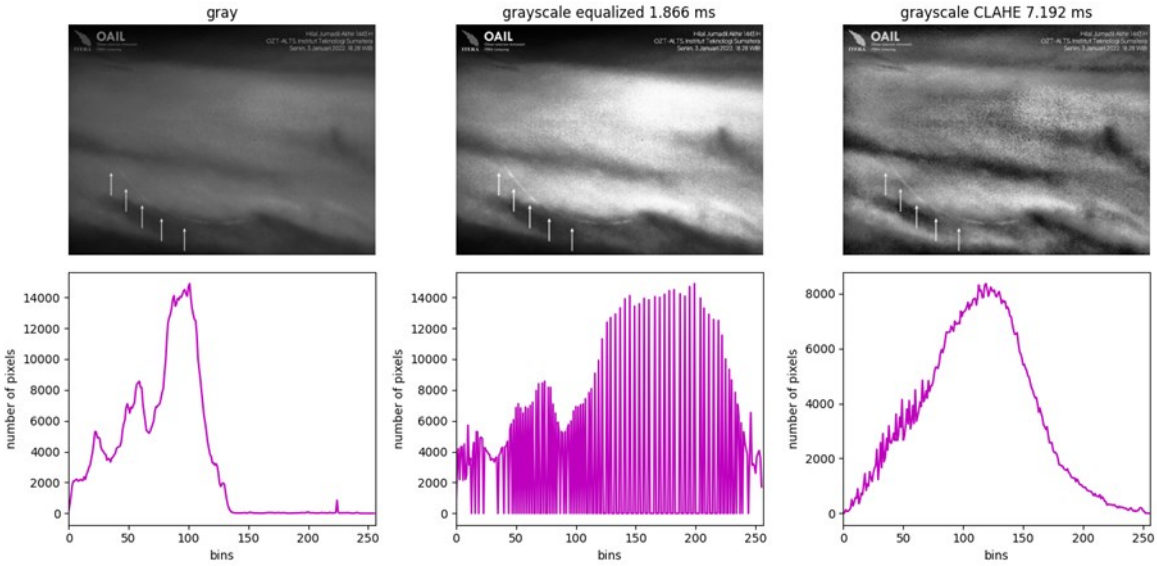

Figure 10. The results of crescent moon observations obtained after sunset. The top is an image taken through the telescope, while the bottom is a histogram of each image. The top-left image is a grayscale version captured outside the camera. The top-middle image shows the results of histogram equalization (HE), and the top-right image shows the results of applying the CLAHE method.

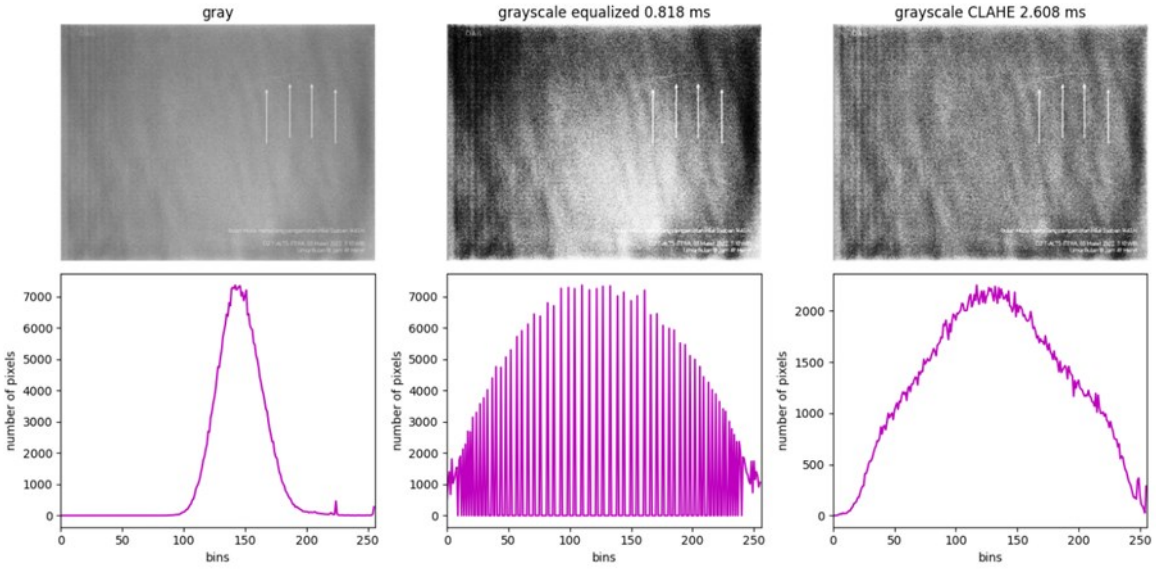

Figure 11. The results of crescent moon observations obtained in daylight. The top is image taken through the telescope, while the bottom is the histogram of each image. The top-left image is a grayscale version captured outside the camera. The top-middle image shows the results of histogram equalization (HE), and the top-right image shows the results of applying the CLAHE method.

the pixel intensity value) as a function of the signal intensity (average pixel intensity value) produced by a flat image (Figure 6). The main objective of photon transfer analysis is to calculate the conversion factor (K) that relates the photo-electrons (e-) in the chip to the grayscale value (GV) in the resulting image (that is, K = e- / GV). From the value of the correction factor obtained, we can derive the CCD characteristic parameters. We used 16 flat images varying from 1 to 50 sec.

According to the technical specifications of the camera manufacturer, the Manta G-031B has a pixel size of 5.6 microns and can be operated at a full capacity value of 14508 e-/pix. Then, the results of the A/D conversion with 12-bit capability have output values from 0 to 4096, so that an empirical

gain of 14508/4096 = 3.5 is obtained. Therefore, setting the gain on the camera at 3.5 e-/ADU is the limit for the CCD to be able to produce good-quality output images by utilizing the entire dynamic range without saturation. The CCD parameters derived from the results of the photon transfer curve can be seen in Table 1.

Figure 7 shows the linearity curve of the flat image measurement results, indicating that the camera has a linear response to incoming photons in most of the dynamic range. As previously mentioned, the Manta G-031B camera has a maximum dynamic range of 3.5 e-/ADU, so in measurements with variations in gain settings of 0 and 2 on the camera device, it is still smaller than the maximum range. Hence, the resulting curve shows the response, which is linear to the number of incoming photons with a longer integration time (longer exposure time). However, if the gain setting exceeds 3.5 e-/ADU, the curve will quickly become nonlinear, even at a short integration time.

The dark current for CCDs is usually specified as the number of thermal electrons generated per sec per pixel or as the actual current generated per device area (i.e., picoamps cm^{-2}). At room temperature, the dark current of a CCD is generally close to 2.5×10^{4} e-/pix/sec. Typical values for properly cooled devices range from 2 e-/sec/pix down to deficient levels of about 0.04 e-/sec/pix. The amount of dark current that a CCD produces depends primarily on its operating temperature, but there is a secondary dependence on the properties of the bulk of the silicon used in its manufacture.

The Manta G-031B camera is specifically designed to have a high frame rate of up to 120 frames/sec. Therefore, this camera is not equipped with a particular cooling component. However, the aluminium material that houses the CCD chip is

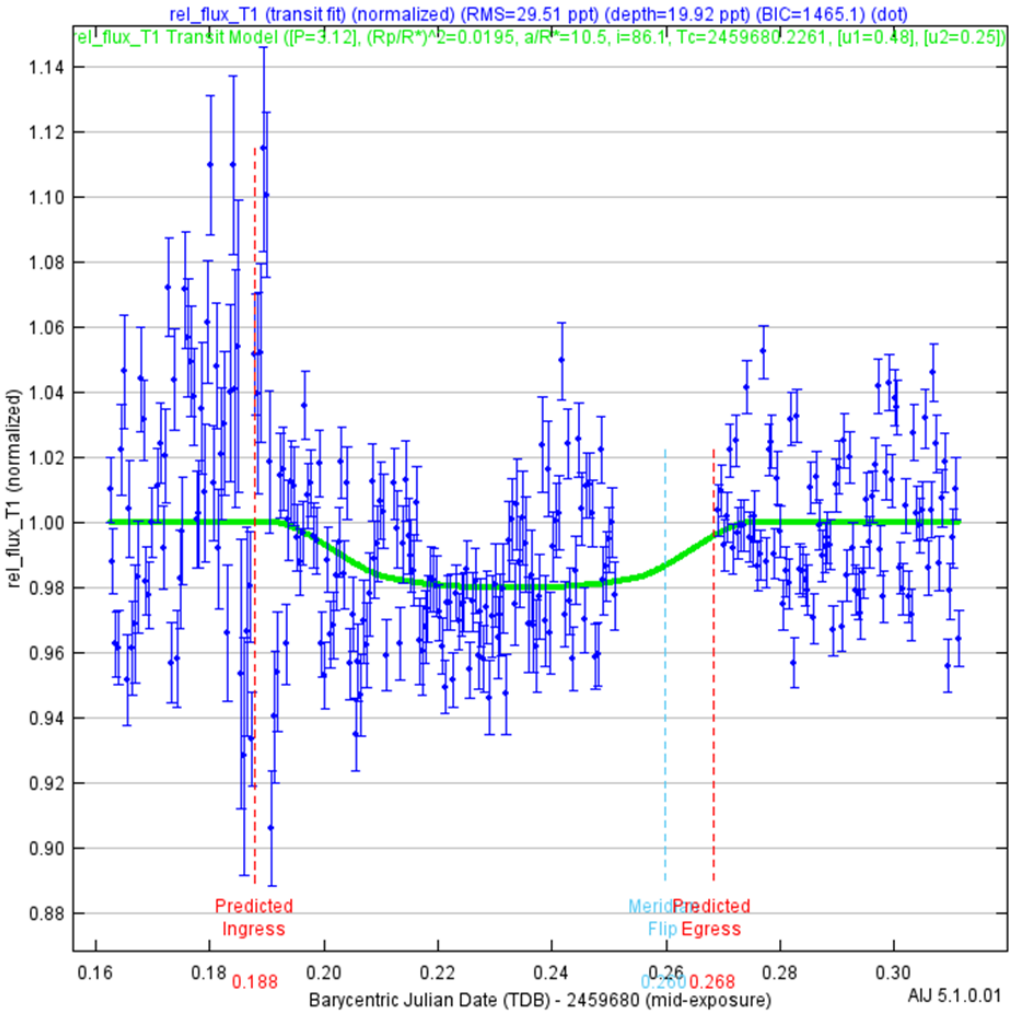

Figure 12. WASP-16 (T1, green colour) with comparison stars (red), along with best fit theoretical light curve for a model of WASP-16b.

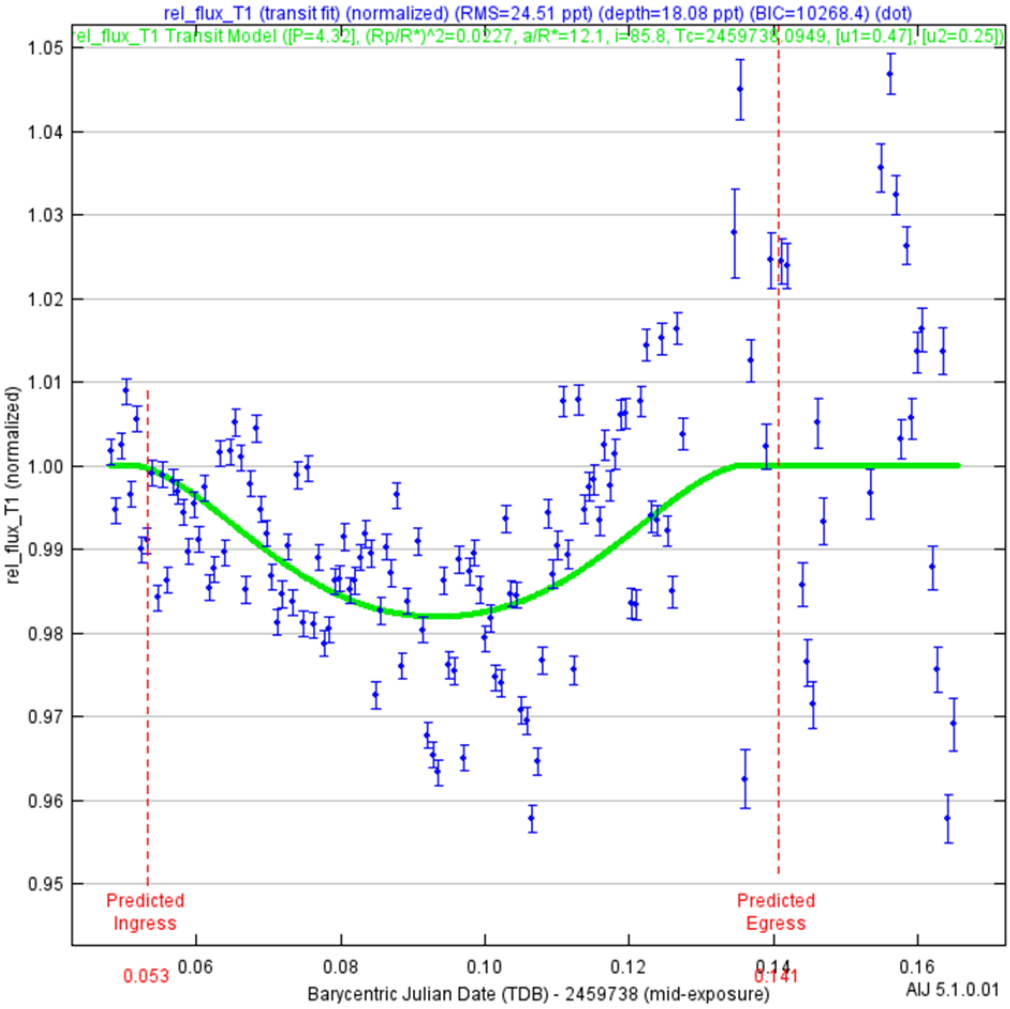

Figure 13. WASP-34 (T1, green color) with comparison stars (red) along with the best fit theoretical light curve for model of WASP-34b.

quite capable of making the camera work optimally at ambient temperatures. This is evident from the measurement results we obtained. The dark current is measured at night when the dome is closed, the lens cover is closed, and the camera is closed to prevent any light from entering. The dark current curve can be seen in Figure 8. The measurement results obtained a dark current value of 5.5 e-/pix/sec. For detailed results of parameter measurements of dark currents (Table 2). The probabilities tend to concentrate on hot pixels; therefore, it is essential to use dark images in image reduction techniques. However, it would be better to use a CCD equipped with a cooling system for more specific astronomical observations, such as observing stars, nebulae, galaxies, and other objects. Technically, the dark current value can also be minimized by lowering the CCD temperature before use. CCD cooling can reduce unwanted electron sources because these non-specific electrons will occupy the potential well space, thereby reducing the dynamic range of the camera itself and producing less than best-quality images.

The last discussion is about the signal-to-noise ratio (SNR). Basically, the most significant noise contributor comes from the photon exposure itself, which obeys Poisson statistics. Therefore, SNR is very limited by the size of the full well capacity or the ability of the potential well to accommodate electrons. As previously explained, the Manta G-031B camera is not equipped with a temperature drop setting. According to the factory specification data, this camera has a temperature range of -10 to 70 °C, but when the camera is being operated, the temperature ranges from 5 to 45 °C. The difference is quite significant compared to today's newest CCD cameras, which can reach -40 °C. Figure 9 shows the results of the SNR measurement plotted

against the average signal value. The graph shows that the SNR value can be increased by an A/D conversion factor with more quantization levels (an increase in quantization depends on an increase in exposure time) or by decreasing the gain setting on the camera device. It should be noted that the reduction in device gain has certain limitations; if the number of electrons received exceeds the full well capacity, SNR will decrease.

3.2. Scientific Observations

3.2.1. Crescent Observation

Since 2022, the ITERA Astronomy Observatory Lampung (OAIL), Sumatra Institute of Technology, has been observing the crescent moon with the OZT -ALTS robotic telescope. Our motivation for collecting crescent data throughout the year is to analyze the position and time when the young crescent was first sighted. The collected data can be used to correct the Islamic calendar system in the future. Furthermore, in collaboration with the Ministry of Religion, the crescent observation was designated as a special mission to provide evidence through a digital image that the first crescent was seen after the new moon for Muslims. The OZT-ALTS robotic telescope is equipped with a camera that is very sensitive to dim light and is integrated with an RG-1000 filter to bypass NIR wavelengths, allowing it to detect the crescent both for observations at sunset and during daytime observations. The OZT-ALTS robotic telescope also has a baffle to improve the contrast of the crescent image. Baffles are used to cut down on stray light from the environment. Furthermore, the high-accuracy performance of the German NTM-500 equatorial mount ensures that the crescent moon object is always visible in the camera's field-of-view.

Following are the results of the crescent moon image taken on January 3, 2022, after sunset at 11 h 28 m UTC with an illumination of 0.7% and an elongation of +05° 42' 45" (Figure 10), and the result of a crescent observation in daylight taken on March 3, 2022, at 04 h 10 m UTC with an illumination of 0.4% and elongation of 07° 20' 20" (Figure 11). We increased the image contrast from the crescent observations so that objects could be seen clearly. We use the Histogram Equalization (HE) and Contrast Limited Adaptive Histogram Equalization (CLAHE) methods on the openCV module for fast image processing. HE distributes pixels evenly across all levels, resulting in a uniform distribution of grey levels for the resulting image. However, in the end, much noise is generated with this technique. CLAHE is operated by dividing the image into tiny blocks or tiles. For each tile, it applies histogram equalization and enhances the contrast in smaller regions, which helps to improve local details. For a crescent moon, this can help bring out finer details in a crescent shape that might otherwise be fainter in a not

Table 3 Comparison result for WASP-34b and WASP-16b exoplanet parameter.

Parameter	WASP-34b		WASP-16b	
	Literature Study	**Our Result**	**Literature Study**	**Our Result**
$Rp/R*$	0.1123 ± 0.0161 [12]	0.1506	0.1144 ± 0.0022 [11]	0.146
$a/R*$	12.07 ± 1.58 [9]	12.07	8.84 ± 0.33 [11]	10.5
e	0.04 ± 0.01 [9][12]	-	> 0.018 [10]	-
i (deg)	85.2 ± 0.20 [9][10][12]	85.8	85.22 ± 0.27 [10]	86.09
P (days)	4.318 ± 0,000005 [8]-[10][12]	-	3.118 ± 0,000001 [11]	-
ω (deg)	-40.2 $^{+23.2}_{-18.6}$ [12]	-	97 $^{+44}_{-20}$ [8]	
b	0.904 $^{+0.017}_{-0.014}$ [12]	0.875	0.81 $^{+0.002}_{-0.04}$ [11]	0.71

uniform histogram image. Since CLAHE adjusts local contrast and focuses on the object region, it can handle differences in contrast between crescent moon objects and the sky background. This means that if some areas of the crescent moon seem fainter than others, CLAHE can enhance the contrast in the crescent moon area without overexposing the brighter areas, resulting in a more balanced and informative image. Meanwhile, CLAHE results show superiority in preserving detail and significantly improving image quality. We are confident that the OZT - ALTS robotic telescope has impressive features for continuously monitoring moon sightings in real time.

3.2.2. Exoplanet Observation

We extensively studied the transiting exoplanets WASP-16b and WASP-34b using the OZT-ALTS robotic telescope. The transit method is particularly useful for calculating the radius of an exoplanet by measuring the change flux ratio when exoplanets pass in front of a host star as seen from Earth. After obtaining a light curve, we use fitting models to analyse characteristics such as orbital motions and radius exoplanets. The size of the host star and the planet will determine the decrease in flux during the transit. Table 3 confirms and compares their physical parameter data to the literature study. The WASP-16b and WASP-34b light curves of the exoplanets can be seen in Figures 12 and 13, respectively.

4. CONCLUSIONS

We have described the design and performance of the OZT-ALTS robotic telescope at the OAIL, Institut Teknologi Sumatera, Lampung, Indonesia. This facility is primarily used for monitoring moon sightings, but it can also be used for advanced research. Based on observation, the results show that the OZT-ALTS robotic telescope is capable of not only monitoring moons but also detecting exoplanets, though with limitations to bright stars (brighter than 11 magnitudes) to allow for shorter exposure times and more frequent data collection. We present examples of transit studies of the exoplanets WASP-36b and WASP-34b conducted with the OZT-ALTS robotic telescope. The optical parts of the refracting telescope use apochromatic lens technology for reducing the effect of wave-front aberration and are outfitted with baffle used to cut down on stray light from the environment, and also an infrared channel filter in front of the CCD camera. So, the system can improve the contrast between a very faint lunar crescent image and the sky background. The CCD camera operates at ambient or room temperature, which may be appropriate for observing the first crescent moon. For the implementation to observe other celestial objects such as variable stars, exoplanets, or other transient celestial objects, the cooled CCD camera with the standard filter systems may be needed for an alternative use for a better improvement of the S/N ratio of the faint celestial objects. The facility also serves as a valuable teaching resource and is used regularly for undergraduate projects at the Institut Teknologi Sumatera.

AUTHOR INFORMATION

Corresponding Author

Hakim L. Malasan — Department of Astronomy and Bosscha Observatory, Institut Teknologi Bandung, Bandung-40132 (Indonesia); Department of Atmospheric and Planetary Sciences, Institut Teknologi Sumatera, Lampung Selatan-35365 (Indonesia);
orcid.org/0000-0001-8549-1811
Email: malasan@itb.ac.id

Authors

Robiatul Muztaba — Departement of Atmospheric & Planetary Sciences, Institut Teknologi Sumatera, Lampung Selatan-35365 (Indonesia);
orcid.org/0000-0002-0043-8796

Aditya Abdillah Yusuf — Observatorium Astronomy ITERA Lampung (OAIL), Institut Teknologi Sumatera, Lampung Selatan-35365 (Indonesia);
orcid.org/0009-0005-5288-2644

Adhitya Oktaviandra — Observatorium Astronomy ITERA Lampung (OAIL), Institut Teknologi Sumatera, Lampung Selatan-35365 (Indonesia);
orcid.org/0009-0008-0631-9502

Mitra Djamal — Department of Physics, Institut Teknologi Bandung, Bandung-40132

(Indonesia);
orcid.org/0000-0002-4698-2949
Tulin Bedel — ASTELCO Systems GmbH, München-81379 (Germany);
orcid.org/0009-0002-4429-236X
Peter Aniol — ASTELCO Systems GmbH, München-81379 (Germany);
orcid.org/0000-0001-8600-8086

Author Contributions

Conceptualization, Writing – Original Draft Preparation and Formal Analysis, H. L. M. and R. M.; Methodology, Software, Validation, and Hardware Development, A. A. Y. and A. O.; Robotic Telescope Installation, Training, and Supervision, T. B., M. D. and P. A.

Conflicts of Interest

The authors declare no conflict of interest.

ACKNOWLEDGEMENT

We are grateful to Mr. Mario Constantine and staff of Astelco Sys., Germany, who have shared ALTS's instruments technical specification, in particular Mr. Joseph Huber and Mrs. Tülin Bedel who supervised staff of OAIL during dome and telescope installation in 2021. Publication of this paper would not possible without substantial fincancial support from Leids-Kerkhoven Bosscha Foundation (LKBF). We thank Director of Bosscha Observatory ITB for facilitating this support. We are grateful to Mr. Sulthan Djumari, and especially to Ms. Nadya Luthfiah have shared several results of exoplanet observation. For a detailed explanation about the exoplanet analysis, please refer to Ms. Luthfiah's B.Sc. thesis at the Department of Atmospheric and Planetary Science, ITERA.

REFERENCES

[1] B. Moomaw. (2013). "Camera technologies for low light imaging: overview and relative advantages". *Methods in Cell Biology.* **114** : 243-83. 10.1016/B978-0-12-407761-4.00011-7.

[2] Stelzer. (2008). "Contrast, resolution, pixelation, dynamic range and signal-to-noise ratio: fundamental limits to resolution in fluorescence light microscopy". *Journal of Microscopy.* **189** (1): 15-24. 10.1046/j.1365-2818.1998.00290.x.

[3] R. Muztaba, H. L. Malasan, and M. Djamal. (2022). "Development of an automated Moon observation system using the ALTS-07 Robotic Telescope: 2. Progress report on standard contrast enhancement of Moon crescent image with OpenCV". *Journal of Physics: Conference Series.* **2214** (1). 10.1088/1742-6596/2214/1/012004.

[4] R. Muztaba, H. L. Malasan, and M. Djamal. (2023). "Deep learning for crescent detection and recognition: Implementation of Mask R-CNN to the observational Lunar dataset collected with the Robotic Lunar Telescope System". *Astronomy and Computing.* **45**. 10.1016/j.ascom.2023.100757.

[5] T. A. Lister, D. R. Anderson, M. Gillon, L. Hebb, B. S. Smalley, A. H. M. J. Triaud, A. Collier Cameron, D. M. Wilson, R. G. West, S. J. Bentley, D. J. Christian, R. Enoch, C. A. Haswell, C. Hellier, K. Horne, J. Irwin, Y. C. Joshi, S. R. Kane, M. Mayor, P. F. L. Maxted, A. J. Norton, N. Parley, F. Pepe, D. Pollacco, D. Queloz, R. Ryans, D. Segransan, I. Skillen, R. A. Street, I. Todd, S. Udry, and P. J. Wheatley. (2009). "WASP-16B: A New Jupiter-Like Planet Transiting A Southern Solar Analog". *The Astrophysical Journal.* **703** (1): 752-756. 10.1088/0004-637x/703/1/752.

[6] J. Southworth, L. Mancini, P. Browne, M. Burgdorf, S. Calchi Novati, M. Dominik, T. Gerner, T. C. Hinse, U. G. Jørgensen, N. Kains, D. Ricci, S. Schäfer, F. Schönebeck, J. Tregloan-Reed, K. A. Alsubai, V. Bozza, G. Chen, P. Dodds, S. Dreizler, X. S. Fang, F. Finet, S. H. Gu, S. Hardis, K. Harpsøe, T. Henning, M. Hundertmark, J. Jessen-Hansen, E. Kerins, H. Kjeldsen, C. Liebig, M. N. Lund, M. Lundkvist, M. Mathiasen, N. Nikolov, M. T. Penny, S. Proft, S. Rahvar, K. Sahu, G. Scarpetta, J. Skottfelt, C. Snodgrass, J. Surdej, and O. Wertz. (2013). "High-precision photometry by telescope defocusing – V. WASP-15 and WASP-

16□". *Monthly Notices of the Royal Astronomical Society.* **434** (2): 1300-1308. 10.1093/mnras/stt1089.

[7] H. A. Knutson, B. J. Fulton, B. T. Montet, M. Kao, H. Ngo, A. W. Howard, J. R. Crepp, S. Hinkley, G. Á. Bakos, K. Batygin, J. A. Johnson, T. D. Morton, and P. S. Muirhead. (2014). "Friends of Hot Jupiters. I. A Radial Velocity Search for Massive, Long-Period Companions to Close-in Gas Giant Planets". *The Astrophysical Journal.* **785** (2). 10.1088/0004-637x/785/2/126.

[8] K. G. Stassun, K. A. Collins, and B. S. Gaudi. (2017). "Accurate Empirical Radii and Masses of Planets and Their Host Stars with Gaia Parallaxes". *The Astronomical Journal.* **153** (3). 10.3847/1538-3881/aa5df3.

[9] A. S. Bonomo, S. Desidera, S. Benatti, F. Borsa, S. Crespi, M. Damasso, A. F. Lanza, A. Sozzetti, G. Lodato, F. Marzari, C. Boccato, R. U. Claudi, R. Cosentino, E. Covino, R. Gratton, A. Maggio, G. Micela, E. Molinari, I. Pagano, G. Piotto, E. Poretti, R. Smareglia, L. Affer, K. Biazzo, A. Bignamini, M. Esposito, P. Giacobbe, G. Hébrard, L. Malavolta, J. Maldonado, L. Mancini, A. Martinez Fiorenzano, S. Masiero, V. Nascimbeni, M. Pedani, M. Rainer, and G. Scandariato. (2017). "The GAPS Programme with HARPS-N at TNG". *Astronomy & Astrophysics.* **602**. 10.1051/0004-6361/201629882.

[10] J. A. Patel and N. Espinoza. (2022). "Empirical Limb-darkening Coefficients and Transit Parameters of Known Exoplanets from TESS". *The Astronomical Journal.* **163** (5). 10.3847/1538-3881/ac5f55.

[11] B. Smalley, D. R. Anderson, A. Collier Cameron, C. Hellier, M. Lendl, P. F. L. Maxted, D. Queloz, A. H. M. J. Triaud, R. G. West, S. J. Bentley, B. Enoch, M. Gillon, T. A. Lister, F. Pepe, D. Pollacco, D. Segransan, A. M. S. Smith, J. Southworth, S. Udry, P. J. Wheatley, P. L. Wood, and J. Bento. (2011). "WASP-34b: a near-grazing transiting sub-Jupiter-mass exoplanet in a hierarchical triple system". *Astronomy & Astrophysics.* **526**. 10.1051/0004-6361/201015992.

[12] E. L. Dereniak, J. Janesick, K. N. Prettyjohns, K. Klaasen, and T. Elliott. (1985). "CCD Charge Collection Efficiency And The Photon Transfer Technique". Presented at the Solid-State Imaging Arrays. 10.1117/12.950297.

[13] J. R. Janesick. (2007). "Photon Transfer". 10.1117/3.725073.

[14] T. M. C. Abbott. (1995) ."In situ CCD testing". Tabla Vii Secciones Utilizadas Para La Estadistica.